

# Sr<sub>2</sub>FeIrO<sub>4</sub>: Square-Planar Ir(II) in an Extended Oxide

Jacob E. Page<sup>†</sup>, Harry W. T. Morgan,<sup>†</sup> Dihao Zeng<sup>†</sup>, Pascal Manuel<sup>‡</sup>, John E. McGrady<sup>†</sup> and Michael A. Hayward<sup>†\*</sup>

<sup>†</sup> Department of Chemistry, University of Oxford, Inorganic Chemistry Laboratory, South Parks Road, Oxford, OX1 3QR, U.K.

<sup>‡</sup> ISIS Facility, Rutherford Appleton Laboratory, Chilton, Oxon OX11 0QX, U.K.

---

**ABSTRACT:** Topochemical reduction of the double-perovskite oxide Sr<sub>2</sub>FeIrO<sub>6</sub> under dilute hydrogen leads to the formation of Sr<sub>2</sub>FeIrO<sub>4</sub>. This phase consists of ordered infinite sheets of apex-linked Fe<sup>2+</sup>O<sub>4</sub> and Ir<sup>2+</sup>O<sub>4</sub> squares, stacked with Sr<sup>2+</sup> cations, and is the first report of Ir<sup>2+</sup> in an extended oxide phase. Plane-wave DFT calculations indicate high-spin Fe<sup>2+</sup> ( $d^6$ ,  $S = 2$ ) and low-spin Ir<sup>2+</sup> ( $d^7$ ,  $S = 1/2$ ) configurations for the metals and confirm that both ions have a doubly occupied  $d_{z^2}$  orbital, a configuration that is emerging as a consistent feature of all layered oxide phases of this type. The stability and double occupation of  $d_{z^2}$  in the Ir<sup>2+</sup> ions invites a somewhat unexpected analogy to the extensively studied Ir<sup>4+</sup> ion as both ions share a common near-degenerate ( $d_{xy/xz/yz}$ )<sup>5</sup> valence configuration. On cooling below 115 K Sr<sub>2</sub>FeIrO<sub>4</sub> enters a magnetically ordered state in which the Ir and Fe sub-lattices adopt type II antiferromagnetically coupled networks which interpenetrate each other leading to frustration in the nearest-neighbor Fe-O-Ir couplings, half of which are ferromagnetic and half anti-ferromagnetic. The spin frustration drives a symmetry-lowering structural distortion in which the four equivalent Ir-O and Fe-O distances of the tetragonal  $I4/mmm$  lattice split into two mutually *trans* pairs in a lattice with monoclinic  $I112/m$  symmetry. This strong magneto-lattice coupling arises from the novel local electronic configurations of the Fe<sup>2+</sup> and Ir<sup>2+</sup> cations and their cation-ordered arrangement in a distorted perovskite lattice.

---

## Introduction

A<sub>2</sub>BB'O<sub>6</sub> double perovskite oxides containing ordered arrays of 3d (B) and 5d (B') transition-metal cations present a rich framework for the study of complex electronic and magnetic phenomena.<sup>1</sup> The two series of transition-metal elements have contrasting features when located in extended oxide lattices: the compact 3d orbitals of the first transition series lead to narrow bands and strong electron-electron correlations while the more extended 5d orbitals of the third series favor wider bands and therefore electron delocalization, but also experience stronger spin-orbit coupling. The subtle interplay between these factors means that when 3d and 5d metals are ordered in extended frameworks, compounds can be prepared with physical properties unlike those of phases containing only 3d or only 5d transition-metal centers. For example in systems such as Sr<sub>2</sub>FeReO<sub>6</sub> where there are itinerant electrons, half-metallic behavior and spin-polarized conductivity can be observed,<sup>2-3</sup> while in insulators the magnetic coupling interactions appear to be dominated by long-range next-nearest neighbor interactions ("super-superexchange") rather than the nearest-neighbor superexchange couplings that are central to the Goodenough-Kanamori rules.<sup>4-6</sup> A further layer of complexity arises because the B and B' cations are arranged in a face-centered cubic array in the undistorted aristotype A<sub>2</sub>BB'O<sub>6</sub> double perovskite lattice, as a result of which they are susceptible to magnetic frustration if either of the B-B or B'-B' couplings is antiferromagnetic. These inter-cation couplings, and therefore the physical behavior of double perov-

skite oxides, can be tuned by modifying the composition, most obviously through the selection of the magnetic cations B and B' but also, more subtly, through the choice of A-cation. These are typically divalent group II metals (Ca<sup>2+</sup>, Sr<sup>2+</sup>, Ba<sup>2+</sup>) or trivalent rare earths (Lanthanide, Y) and their size and charge can have a decisive influence on the physical behavior of phases because the average A-cation charge controls B-cation oxidation states while the average A-cation size controls the cooperative 'tilting' distortions of the perovskite network. This second effect, where the BO<sub>6</sub> and B'O<sub>6</sub> units undergo cooperative rotations to accommodate the A-cations in the 12-coordinate cavities within the perovskite network, can be used to tune the B-O-B' bond angles and thus the B-B' electronic couplings.<sup>7-8</sup> As an illustration, we note that substitution of calcium for strontium in A<sub>2</sub>FeOsO<sub>6</sub> drives a change from antiferromagnetic to ferrimagnetic order, associated with a change in the tilting pattern of the FeO<sub>6</sub> and OsO<sub>6</sub> octahedra.<sup>9</sup> Similarly, calcium-for-strontium substitution in A<sub>2</sub>FeReO<sub>6</sub> drives a change from metallic to insulating behavior, an effect that is again correlated with a change in the Fe-O-Re bond angles.<sup>10-11</sup>

Topochemical reductions offer a further opportunity to modify the interactions between the magnetic ions in double perovskite oxides. By deintercalating oxide ions from perovskite lattices in structure conserving reactions, the oxidation states and local coordination environments of the transition metals can be modified, often to the point where they adopt electronic configurations that are completely inaccessible un-

der typical high-temperature synthetic conditions. For example, phases containing octahedral  $\text{Mn}^{1+}$  and square-planar  $\text{Ni}^{1+}$ ,  $\text{Co}^{1+}$ ,  $\text{Ru}^{2+}$  or  $\text{Fe}^{2+}$  have all been prepared using binary metal hydrides as reducing agents.<sup>12–16</sup> The combination of unusually low oxidation states and/or unusual coordination geometries gives rise to inter-cation couplings that often differ substantially from those in the unreduced parent phases. We have recently demonstrated the reduction of the B-cation ordered double perovskite  $\text{LaSrNiRuO}_6$  yields the infinite-layer phase  $\text{LaSrNiRuO}_4$ , with retention of the B-cation order of the ‘parent’ phase.<sup>17</sup> Here we describe the analogous reduction of the  $3d/5d$  double perovskite  $\text{Sr}_2\text{FeIrO}_6$  to  $\text{Sr}_2\text{FeIrO}_4$ , the first extended oxide to contain iridium in the remarkably low +2 oxidation state. The unusual square-planar coordination geometry at  $\text{Ir}^{2+}$  gives rise to a doublet state with near 3-fold orbital degeneracy, as a result of which its electronic properties bear a surprising resemblance to the octahedral iridates ( $\text{Ir}^{4+}$ ) despite the difference of two in the oxidation state.

## Experimental

**Synthesis of  $\text{Sr}_2\text{FeIrO}_6$ .** Samples of  $\text{Sr}_2\text{FeIrO}_6$  were prepared using a citrate gel method.<sup>18</sup> Appropriate quantities of  $\text{SrCO}_3$  (99.994%) and Fe (99.99%) were dissolved in a 1:1 mixture of concentrated nitric acid and distilled water, then the required amount of  $\text{IrO}_2$  (99.99%, dried at 700 °C for 2 hours) was added. Citric acid and analar ethylene glycol were added and the solution was heated whilst being stirred. The gel thus formed was allowed to combust in air and the subsequent product was ground into a fine powder, placed in an alumina crucible and heated in air, at a rate of 1 °C min<sup>-1</sup> to 1000 °C, to remove the organic components from the sample. The resulting powder was pressed into pellets and heated in air for two periods of two days at 1100 °C. Synchrotron X-ray powder diffraction data collected from  $\text{Sr}_2\text{FeIrO}_6$  could be indexed using a triclinic unit cell (space group  $\bar{1}$ ) with lattice parameters  $a = 5.55332(6)$  Å,  $b = 5.58023(6)$  Å,  $c = 7.84643(2)$  Å,  $\alpha = 89.968(2)^\circ$ ,  $\beta = 90.069(2)^\circ$ ,  $\gamma = 90.107(1)^\circ$ , with refinements indicating 7% anti-site disorder between the iron and iridium cations, in good agreement with values previously reported in the literature.<sup>18–19</sup>

**Reduction of  $\text{Sr}_2\text{FeIrO}_6$ .** Small-scale tests to assess the reactivity of  $\text{Sr}_2\text{FeIrO}_6$  were performed by heating samples under flowing 5%/95%  $\text{H}_2/\text{N}_2$  in the temperature range 300 <  $T$ /°C < 420. A sample for analysis by neutron powder diffraction was prepared by reacting approximately 1.25g of  $\text{Sr}_2\text{FeIrO}_6$  with flowing 5%/95%  $\text{H}_2/\text{N}_2$  at 390 °C for 4 periods of 24 hours with regrinding between heating periods.

**Characterization.** X-ray powder diffraction data were collected from samples contained in gas-tight sample holders using a PANalytical X’Pert diffractometer incorporating an X’celerator position sensitive detector (monochromatic Cu  $K_{\alpha 1}$  radiation). High-resolution synchrotron X-ray powder diffraction data were collected using instrument I11 at the Diamond Light Source Ltd. Diffraction patterns were collected using Si-calibrated X-rays with an approximate wavelength 0.825 Å, from samples sealed in 0.3 mm diameter borosilicate glass capillaries. Neutron powder diffraction data were collected using the WISH instrument at the ISIS neutron source, from samples contained within vanadium cans. Rietveld profile refinements were performed using the GSAS suite of programs.<sup>20</sup> DC magnetization data were collected using a Quan-

tum Design MPMS SQUID magnetometer. Thermogravimetric measurements were performed by heating powder samples at a rate of 5 °C min<sup>-1</sup> under an oxygen atmosphere, using a Mettler-Toledo MX1 thermogravimetric microbalance.

**Computational methods.** All density functional theory calculations were carried out using the VASP software package,<sup>21,22</sup> version 5.3.5, with the PBE functional<sup>23</sup> and a plane-wave cutoff of 450 eV. The effect of the core electrons was incorporated using PAW potentials,<sup>24</sup> and Hubbard  $U_{\text{eff}}$  values of 4.0 eV and 2.0 eV were used for Fe and Ir, respectively.<sup>25</sup> For the smaller  $\sqrt{2} \times \sqrt{2} \times 1$  unit cell, the Brillouin zone was sampled on a range of  $\Gamma$ -centered grids<sup>26</sup> from  $4 \times 4 \times 4$  to  $6 \times 6 \times 6$  while a smaller  $3 \times 3 \times 3$  grid was used for the  $2\sqrt{2} \times 2\sqrt{2} \times 1$  unit cell. Spin-orbit coupling is included<sup>27</sup> using a variety of orientations of the quantization axis ((1,0,0), (0,1,0), (0,0,1), (1,1,0), (1,0,1) and (1,1,1)): the lowest energy solution corresponds to a quantization axis lying in the  $xy$  plane.

## Results and discussion

**Chemical reactivity and stability.** Small-scale tests, monitored by X-ray powder diffraction, showed no reaction between  $\text{Sr}_2\text{FeIrO}_6$  and flowing 5%/95%  $\text{H}_2/\text{N}_2$  at temperatures below 380 °C. In the temperature range 380 <  $T$ /°C < 400 a new phase was observed to form, which could be indexed approximately on the basis of a tetragonal unit cell with lattice parameters  $a = 5.64$  Å and  $c = 7.08$  Å. Reactions at temperatures above 400 °C resulted in decomposition of the sample to binary oxides and elemental iridium. Thermogravimetric measurements performed by heating  $\text{Sr}_2\text{FeIrO}_{6-x}$  samples under flowing oxygen to recover  $\text{Sr}_2\text{FeIrO}_{6.0}$  (confirmed by X-ray powder diffraction) indicated mass gains consistent with an original composition of  $\text{Sr}_2\text{FeIrO}_4$  for the reduced phase, as described in the Supporting Information. The  $\text{Sr}_2\text{FeIrO}_4$  phase formed *via* this route proves to be highly metastable, both thermally (decomposing at  $T > 500$  °C) and chemically. The chemical instability of the phase is highlighted by the observation that whilst  $\text{Sr}_2\text{FeIrO}_4$  can also be prepared *via* the reaction of  $\text{Sr}_2\text{FeIrO}_6$  with  $\text{CaH}_2$  (reactivity that is analogous to other  $3d$ - $4d/5d$  double perovskites), all attempts to remove the  $\text{CaO}/\text{CaH}_2$  from reaction products with solutions of  $\text{NH}_4\text{Cl}$  in  $\text{CH}_3\text{OH}$  led to sample decomposition and the formation of large quantities of finely divided elemental iridium. In contrast other topochemically reduced oxides, such as  $\text{SrFeO}_2$ ,  $\text{SrFe}_{0.5}\text{Ru}_{0.5}\text{O}_2$ , or  $\text{LaSrNiRuO}_4$  are stable under the same conditions.<sup>15–17</sup> The modest stability of  $\text{Sr}_2\text{FeIrO}_4$  is unsurprising given the presence of  $\text{Ir}^{2+}$  centers (*vide infra*), a very rare oxidation state for which only a very few mononuclear complexes have been reported.<sup>28–31</sup> This scarcity can be attributed to the ease with which paramagnetic  $d^7$   $\text{Ir}^{2+}$  species can be either oxidized to  $d^6$   $\text{Ir}^{3+}$  or reduced to  $d^8$   $\text{Ir}^{1+}$ , the two oxidation states that dominate iridium chemistry in a molecular context. The fact that  $\text{Sr}_2\text{FeIrO}_4$  can be formed at all by reduction of  $\text{Sr}_2\text{FeIrO}_6$  reflects the ability of the Sr-Fe-O lattice to kinetically stabilize the  $\text{Ir}^{2+}$  centers, preventing further reduction to elemental iridium. We have previously commented on the kinetic stabilization of  $\text{Ru}^{2+}$  in  $\text{SrFe}_{0.5}\text{Ru}_{0.5}\text{O}_2$ , prepared *via* the reduction of  $\text{SrFe}_{0.5}\text{Ru}_{0.5}\text{O}_3$ ,<sup>15</sup> and this new reaction further highlights the ability of  $3d$  transition metals to stabilize the lower oxidation states of  $4d$  and  $5d$  transition metal cations in extended oxide lattices.

**Structural characterization of  $\text{Sr}_2\text{FeIrO}_4$ .** Synchrotron X-ray powder diffraction data collected from  $\text{Sr}_2\text{FeIrO}_4$  at 300 K can be indexed using a body centered tetragonal cell with lattice parameters  $a = 5.6469(1) \text{ \AA}$ ,  $c = 7.0818(2) \text{ \AA}$ . These lattice parameters are very similar to those reported for the tetragonal mixed Ni/Ru layered oxide phase  $\text{LaSrNiRuO}_4$ , suggesting that  $\text{Sr}_2\text{FeIrO}_4$  adopts a similar B-cation ordered infinite layer structure.<sup>17</sup> A structural model was therefore constructed in space group  $I4/mmm$  and refined against the data, yielding a good statistical fit ( $\chi^2 = 5.37$ ), as described in the Supporting information. This, and all other models, incorporated the 7% Fe/Ir anti-site disorder observed in the  $\text{Sr}_2\text{FeIrO}_6$  parent phase, from which the B-cation order is inherited. Close inspection of the data revealed weak additional reflections attributable to  $\text{SrO}$ ,  $\text{Sr}_2\text{Fe}_2\text{O}_5$  and elemental iridium, so these were added as additional phases to the structural model.

Infinite layer phases, like the oxygen-stoichiometric perovskite phases from which they are derived, can undergo a range of low energy structural distortions related to the cooperative twisting and subtle deformation of the constituent  $\text{MO}_4$  units. X-ray diffraction data are not typically very sensitive to these distortions, particularly when they are small in magnitude, as they principally involve the displacement of oxide ions. We have therefore also collected neutron diffraction data from  $\text{Sr}_2\text{FeIrO}_4$  at 150 K to determine accurately the positions of the oxide ions in the reduced phase. As will be shown later,  $\text{Sr}_2\text{FeIrO}_4$  adopts a magnetically ordered structure only below 115 K, and so the data set at 150 K contains only contributions from the nuclear structure, not from the magnetic structure. A series of alternative structural models were constructed which describe the distortions of the infinite layer structure from the  $I4/mmm$  symmetry of the aristotype framework by cooperative rotation of the  $\text{MO}_4$  units and by an ‘orthorhombic’ distortion in which the local symmetry of the  $\text{MO}_4$  units is lowered from  $D_{4h}$  to  $C_{2h}$ , described in detail in the Supporting Information. Refinement of these models against the 150 K neutron diffraction data gave fits which were statistically equivalent, or worse than the high-symmetry  $I4/mmm$  model (Table S2). In addition the positions of atoms in the lower symmetry models refined to locations which were equivalent to their high symmetry sites in the aristotype structure, all of which confirms that  $\text{Sr}_2\text{FeIrO}_4$  does indeed adopt an undistorted tetragonal infinite layer structure at  $T > 150 \text{ K}$ . A representation of the refined structure of  $\text{Sr}_2\text{FeIrO}_4$  is shown in Figure 1, with selected bond lengths and angles listed in Table 1 and plots of the observed and calculated neutron diffraction data are shown in Figure 2. Complete details of the refined structure are given in Table S3 in the Supporting Information. At 150 K, the  $\text{Fe}^{2+}$ -O bond length of  $1.982(4) \text{ \AA}$  is similar to the corresponding value of  $1.995 \text{ \AA}$  in  $\text{SrFeO}_2$ ,<sup>16</sup> while the  $\text{Ir}^{2+}$ -O bond length of  $2.010(4) \text{ \AA}$  is marginally shorter than the corresponding  $\text{Ru}^{2+}$ -O distances in the square planar  $\text{Ru}^{2+}\text{O}_4$  units in  $\text{Sr}_2\text{FeRuO}_4$  and  $\text{LaSrNiRuO}_4$ .

**Low-temperature magnetic and structural characterization.** Zero-field cooled (ZFC) and field cooled (FC) magnetization data collected from  $\text{Sr}_2\text{FeIrO}_4$  in an applied field of 100 Oe are shown in Figure 3. On cooling, the ZFC and FC curves diverge slightly over the temperature range  $300 > T/\text{K} > 115$ , at which point the former goes through a maximum, followed by a more striking divergence below this temperature. Magnetization-field data collected in an applied field of  $\pm 50 \text{ KOe}$

at 300 K are linear and pass through the origin (Figure 4), effectively ruling out the possibility that the observed divergence between ZFC and FC data is due to the presence of elemental iron. Equivalent magnetization-field data become increasingly sigmoidal as the temperature is lowered, with hysteresis observed in data collected below 125 K.

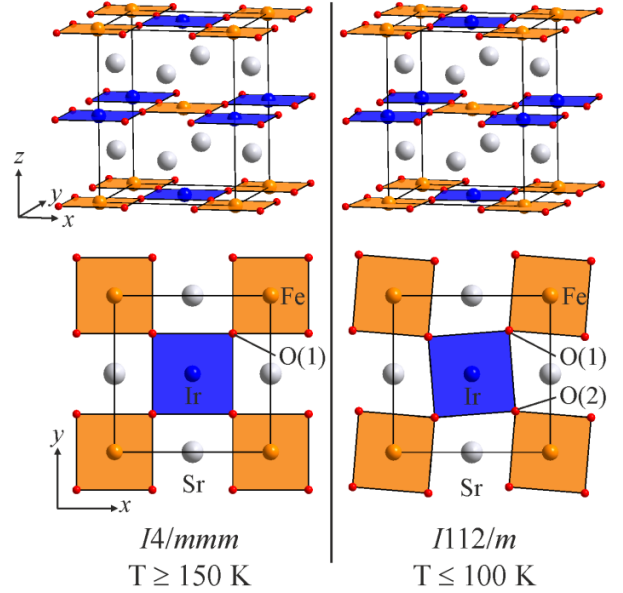


**Figure 1.** The high- and low-temperature structures of  $\text{Sr}_2\text{FeIrO}_4$  shown in projection (top) and highlighting the basal  $\text{FeIrO}_4$  plane (bottom). Gray, red, blue and brown spheres represent Sr, O, Ir and Fe respectively. The magnitude of the distortion to the structure is exaggerated on the  $I112/m$  symmetry figure, to make the orientations of the rotations clearer.

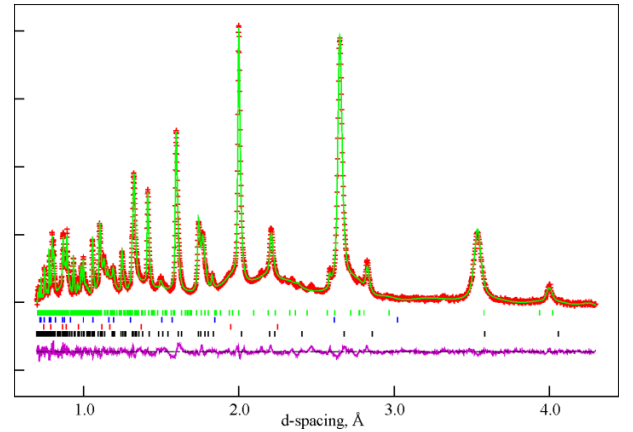


**Figure 2.** Observed, calculated and difference plots from the structural refinement of  $\text{Sr}_2\text{FeIrO}_4$  against neutron diffraction data collected at 150 K. Tick marks indicate peak positions of  $\text{Sr}_2\text{FeIrO}_4$  (bottom), elemental Ir (lower middle),  $\text{SrO}$  (upper middle) and  $\text{Sr}_2\text{Fe}_2\text{O}_5$  (top).

	Bond lengths (Å)		
	150 K	1.5 K	
Cation (M)	M-O	M-O(1)	M-O(2)
Fe	1.982(4)	1.999(7)	1.970(7)
Ir	2.010(4)	1.989(7)	2.026(7)
	Bond Angles (°)		
	150 K	1.5 K	
	Fe-O-Ir	Fe-O(1)-Ir	Fe-O(2)-Ir
	180	177.9(3)	179.7(3)

**Table 1.** Selected bond length and angles from the refined structures of  $\text{Sr}_2\text{FeIrO}_4$  at 150 K and 1.5 K

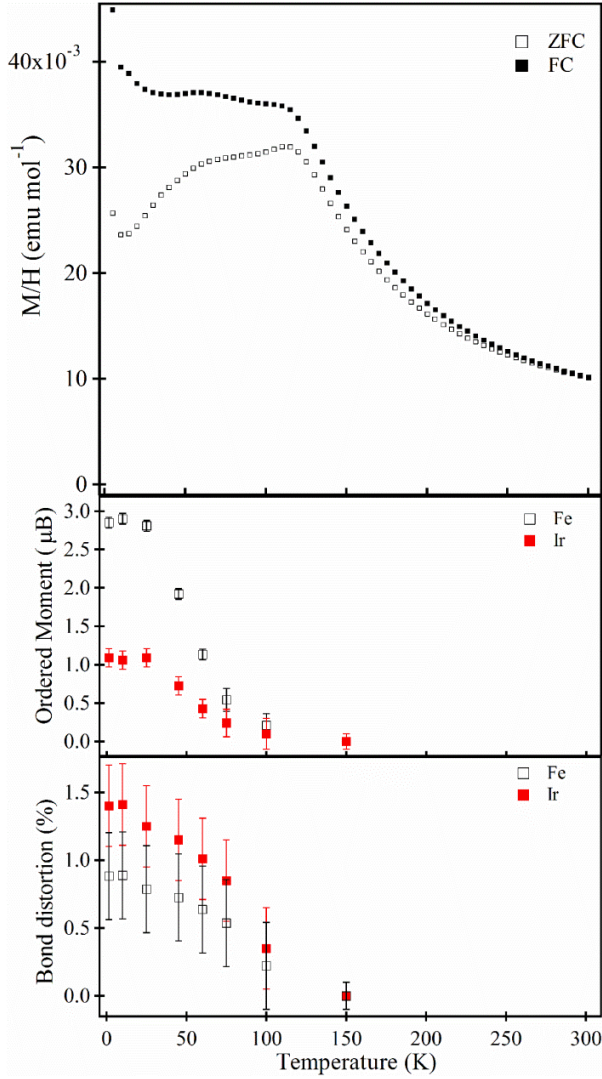


**Figure 3.** Zero-field cooled and field cooled magnetization data collected in an applied field of 100 Oe from  $\text{Sr}_2\text{FeIrO}_4$  (top); ordered magnetic moment on Fe and Ir centers (middle) and bond distortion index defined as  $[[\text{M-O}(1)] - [\text{M-O}(2)]] / [0.5 \times ([\text{M-O}(1)] + [\text{M-O}(2)])]$  (bottom) extracted from fits to neutron diffraction data.

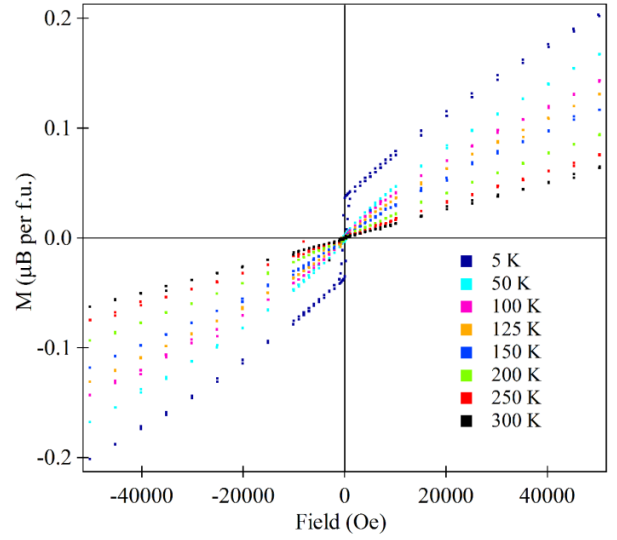


**Figure 4.** Magnetization-field data collected from  $\text{Sr}_2\text{FeIrO}_4$  at temperatures between 300 K and 5 K.

In order to further probe the low temperature behavior of  $\text{Sr}_2\text{FeIrO}_4$ , additional neutron diffraction data were collected at 1.5 K. A comparison of data collected at 1.5 K and 150 K reveals a series of additional diffraction reflections in the low temperature data set (Supporting Information, Figure S4) which can be indexed using a  $\sqrt{2} \times \sqrt{2} \times 2$  expansion of the crystallographic unit cell. A magnetic symmetry analysis was performed on the  $\text{Sr}_2\text{FeIrO}_4$  lattice (space group  $I4/mmm$ ) using the ISODISTORT software,<sup>32</sup> for both the iron and iridium centers, and the results were used to construct a series of trial magnetic structures. These symmetry compatible magnetic models were then refined against the neutron diffraction data collected at 1.5 K, using the iridium magnetic form factor described by Kobayashi *et al.*<sup>33</sup> The magnetic diffraction intensity is best accounted for using the model shown in Figure 5, where both the Fe and Ir lattices are individually Type-II antiferromagnetic ordered, with spins aligned in the  $\text{MO}_4$  planes (ordered moments at 1.5 K: Fe = 2.84(7)  $\mu\text{B}$ ; Ir = 1.09(12)  $\mu\text{B}$ ), as described more fully in the Supporting Information. We note that this is a highly unusual magnetic structure with ferromagnetic Fe-Ir alignments along the  $x$ -axis, and antiferromagnetic alignments along the  $y$ -axis, with alternating antiferromagnetic and ferromagnetic alignments along the  $z$ -axis. However, the only way that the magnetic scattering intensity could be accounted for was by having ordered moments on both the iron and iridium sites. Further neutron diffraction data sets collected on warming reveal that the ordered magnetic moments on both Fe and Ir decline to a value close to zero at 100 K (Figure 3) suggesting that the feature in the magnetization data at 115 K is coincident with the Néel temperature of  $\text{Sr}_2\text{FeIrO}_4$ .

Close inspection of the low-temperature data reveals that in addition to the emergence of magnetic order,  $\text{Sr}_2\text{FeIrO}_4$  also undergoes a symmetry-lowering structural transition in which the  $\text{MO}_4$  planar units undergo both collective rotations about the  $z$ -axis and deformations which break their 4-fold symmetry to yield a structure described in space group  $I112/m$ . A representation of the refined structure of  $\text{Sr}_2\text{FeIrO}_4$  at 1.5 K is shown in Figure 1 (right) with selected bond lengths and an-

gles listed in Table 1. Complete details of the refined crystal and magnetic structures of  $\text{Sr}_2\text{FeIrO}_4$  at 1.5 K are given in Tables S5 and S6 respectively, with plots of the observed and calculated data are shown in Figure S5 in the Supporting Information. We note that the choice of magnetic model did not affect which of the structural models fitted the data best and *vice versa*.

The magnetization data shown in Figure 3 exhibit weak anomalies at  $T \sim 55$  K and  $T \sim 10$  K. These features are not associated with any changes in the neutron diffraction data so we are unable to determine their cause. However we note that samples contain  $\sim 7\%$  Fe/Ir anti-site disorder (inherited from the  $\text{Sr}_2\text{FeIrO}_6$  starting material) which could be the origin of the magnetization anomalies.

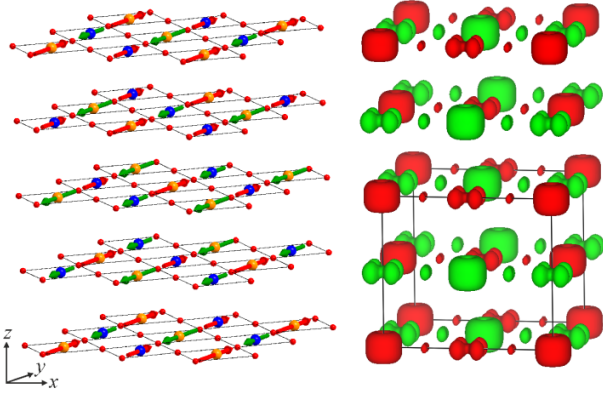


**Figure 5.** The magnetic structure of  $\text{Sr}_2\text{FeIrO}_4$  obtained from neutron diffraction experiments (left) and the computed (collinear) magnetization density (right). Blue, brown and red spheres represent Ir, Fe, and O respectively. In the magnetization density plot, spin- $\alpha$  and spin- $\beta$  densities are shown as green and red, respectively. Note the computational cell is half the volume of the experimental cell, as described in the text.

### Electronic structure analysis

Our initial exploration of the electronic structure was based on spin-unrestricted DFT calculations using a  $\sqrt{2} \times \sqrt{2} \times 1$  expansion of the 1.5 K neutron diffraction structure ( $I112/m$ ) without further geometry optimization. We have also imposed the magnetic structure obtained from the 1.5 K neutron diffraction data, with ferromagnetic chains running along the  $x$  axis and antiferromagnetic chains along  $y$  (this configuration is labelled ‘*stripe*’ in Figure 7). The computed magnetization density plot for this configuration is shown in Figure 5, right, and the converged magnetic moments of  $\pm 3.67$   $\mu\text{B}$  (Fe) and  $\pm 0.67$   $\mu\text{B}$  (Ir), although somewhat larger and smaller, respectively, than the saturated moments obtained from the neutron diffraction study, are nevertheless highly diagnostic of high-spin  $\text{Fe}^{2+}$  ( $d^6$ ,  $S = 2$ ) and low-spin  $\text{Ir}^{2+}$  ( $d^7$ ,  $S = 1/2$ ), respectively. The spin- and orbital-projected density of states (DOS) for this *stripe* configuration is shown in Figure 6. The Fe DOS is typical of square planar  $\text{Fe}^{2+}$  in layered oxide lattices ( $\text{SrFeO}_2$ ,  $\text{Sr}_2\text{FeRuO}_4$ )<sup>16-17</sup>, with the minority-spin electron occupying the  $d_{z^2}$  orbital (the fingerprint of this double occupation is appar-

ent in the depletion of magnetization density along the  $c$  axis for the Fe centers in Figure 5). The projected DOS at Ir shows that  $d_{z^2}$  is again doubly occupied, as are the doubly degenerate  $d_{xz/yz}$  orbitals. This leaves the in-plane  $d_{xy}$  orbital singly occupied, its majority- and minority-spin components straddling the Fermi level. The fingerprint of the  $d_{xy}$  orbital is clearly visible in the collinear magnetization density at Ir in Figure 5. The relative stability of the  $d_{z^2}$  orbital appears to be a very general feature of this class of layered oxide phases, and its origins have been explained in terms of extensive  $s/d_{z^2}$  mixing which increases the average separation between the two electrons.<sup>34</sup> It is important to note, however, that the  $s/d_{z^2}$  mixing mechanism is symmetry allowed for any square planar metal center, whether molecular or in an extended lattice, yet the orbital ordering shown in Figure 6 appears to be restricted to this family of 2-dimensional layered oxides. The unique feature appears to be the presence of eight  $\text{Sr}^{2+}$  cations surrounding the transition metal ions, four above and four below the  $\text{MO}_4$  plane. In the absence of the two oxides that have been extruded from the lattice, these eight  $\text{Sr}^{2+}$  ions generate a positive electrostatic potential in precisely the region occupied by the major lobes of the  $d_{z^2}$  orbitals. In effect, the minority-spin electron moves towards the positive oxide vacancy in the lattice. The unusual electronic configuration therefore appears to be a consequence of the unique electrostatic environment of the metal ions in these layered lattices.

Whatever its origins, the double occupation of the  $d_{z^2}$  orbital in  $\text{Ir}^{2+}$  leaves the remaining five electrons to be distributed over a near-degenerate  $d_{xy/xz/yz}$  orbital triplet. This situation is strikingly similar to the pseudo-octahedral  $\text{Ir}^{4+}$  iridates, and indeed the density of states around the Fermi level shown in Figure 6(a) is remarkably similar to that reported by Felser and co-workers for  $\text{La}_2\text{ZnIrO}_6$ ,<sup>35</sup> with the obvious difference that the  $d_{z^2}$  band lies above the Fermi level in the latter case rather than below it. The iridates have attracted a great deal of attention in the recent literature<sup>36</sup> because the strong spin-orbit coupling at Ir splits the  $\{L = 1, S = 1/2\}$  manifold into distinct  $J = 1/2$  and  $J = 3/2$  spin-orbit states, the  $J = 1/2$  state lying lowest and giving rise to a 1-dimensional Mott-Hubbard band. Motivated by this analogy, we have explored the effects of spin-orbit coupling on the DOS of both Ir and Fe (Figure 6(b)). Comparison with the collinear versions (left) confirms that the total Fe and Ir DOS (*i.e.* the sum of the majority- and minority-spin DOS) is largely unchanged, but there is a small redistribution of Ir  $d$  character, such that the band just above the Fermi level has a small amount of  $d_{xz/yz}$  character (green) in addition to the still dominant  $d_{xy}$  component (red). In terms of the local tetragonal environment, the spin-orbit operator mixes the  ${}^2\text{B}_{1g}$  and  ${}^2\text{E}_g$  states arising from the  $(d_{z^2})^2(d_{xz/yz})^4(d_{xy})^1$  and  $(d_{z^2})^2(d_{xz/yz})^3(d_{xy})^2$  configurations, respectively, both of which transform as  $\Gamma_7^+$  ( $= \text{E}_{3/2g}$ ) in the  $D_{4h}$  double group. The spin orbit coupling generates a finite orbital moment in the  $ab$  plane ( $\mu_L = 0.22$   $\mu\text{B}$ ). We note here that the influence of spin-orbit coupling is critically dependent on the zeroth-order energetic separation of the  $d_{xz/yz}$  and  $d_{xy}$  bands, which in turn depends on both the low-symmetry splitting and the value of the Hubbard parameter  $U_{\text{Ir}}$ , both of which are of the similar magnitude to the intrinsic spin-orbit coupling at iridium. With smaller  $U_{\text{Ir}}$  values of 1.0 or 0.0, the effects of spin-orbit coupling are magnified, the orbital moment increases (to 0.28  $\mu\text{B}$



and 0.38  $\mu_B$ , respectively) and the  $d_{xz/yz}$  character in the band just above the Fermi level increases (the limiting value of

$d_{xz}:d_{yz}:d_{xy}$  character is 1:1:1 for a pure  $J_{1/2}$  state).

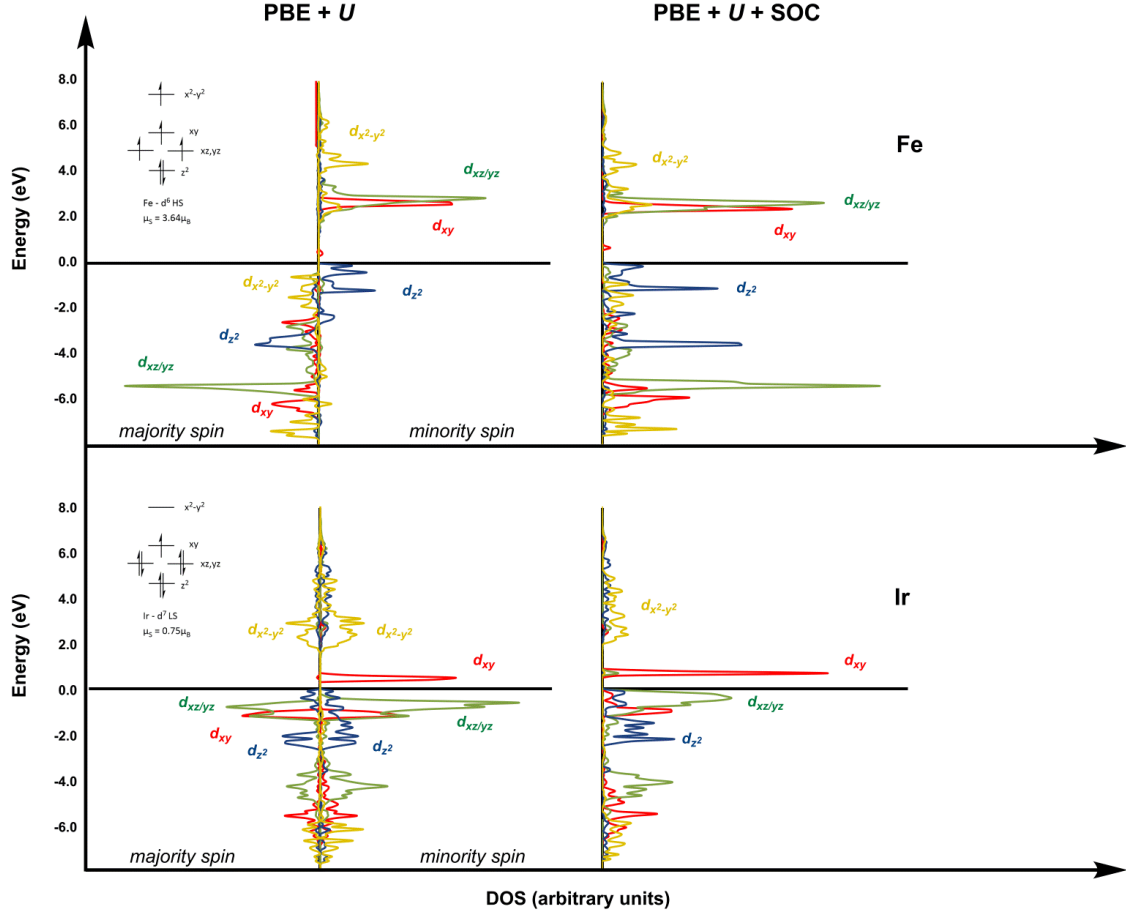


**Figure 6.** Spin- and orbital-projected density of states for Fe and Ir in the *stripe* magnetic configuration shown in Figure 5: (a) PBE +  $U$  ( $U_{Fe} = 4.0$  eV,  $U_{Ir} = 2.0$  eV) and (b) PBE +  $U$  + SOC.

In the preceding qualitative discussion of electronic structure we have imposed the *stripe* magnetic configuration that emerges from the low-temperature neutron diffraction data. In order to explore the origins of this rather unusual arrangement, we have calculated the energies of the seven distinct arrangements of local spins in a  $\sqrt{2} \times \sqrt{2} \times 1$  expansion of the unit cell shown in Figure 7. The DFT-computed energies are then mapped on to the diagonal elements of the Heisenberg spin Hamiltonian with  $S_{Fe} = 2$ ,  $S_{Ir} = 1/2$ :

$$\hat{H}_{HDVV} = - \sum_{i>j} J_{ij} \hat{S}_i \cdot \hat{S}_j$$

Our approach to constructing a suitable spin Hamiltonian is to identify a minimal set of parameters (Figure 7, top) that will yield an acceptable fit to the DFT energies. A 4-parameter Hamiltonian which includes the nearest-neighbor (NN) Fe-Ir couplings in the  $xy$ -plane ( $J_1$ ) and along the  $z$ -axis ( $J_2$ ), along with coupling between next-nearest neighbor (NNN) Ir ( $J_3$ ) and NNN Fe centers ( $J_4$ ) provides a good fit (root mean squared error = 0.0032 eV with a 663  $\Gamma$ -centered grid, see supporting information, Table S9 for full details of the calculations), with  $J_1 = -44.7$   $\text{cm}^{-1}$ ,  $J_2 = -11.7$   $\text{cm}^{-1}$ ,  $J_3 = -236.0$   $\text{cm}^{-1}$

and  $J_4 = +2.2$   $\text{cm}^{-1}$ . From this analysis it is clear that the dominant contributions to the magnetic order come from the NN Fe-Ir couplings ( $J_1 = -44.7$   $\text{cm}^{-1}$ ) and the NNN Ir-Ir couplings ( $J_3 = -236.0$   $\text{cm}^{-1}$ ), both of which are strongly antiferromagnetic. Strong NNN coupling (“super-superexchange”) is a well-established paradigm in double perovskites and related systems,<sup>37-39</sup> and in this case the highly covalent nature of the Ir–O bonds is clearly significant in mediating the strong  $\text{Ir}(d_{xy})^1\text{--O}(2p)\cdots\text{O}(2p)\text{--Ir}(d_{xy})^1$  interaction ( $J_3$ ). The strongly antiferromagnetic NN Fe-Ir coupling ( $J_1$ ), in contrast, is mediated by  $\text{Fe}(d_{xy})^1\text{--O}(2p)\text{--Ir}(d_{xy})^1$  overlap, as anticipated from the Goodenough-Kanamori rules.<sup>40</sup> The similar energies of the  $d_{xy}$  bands on the two metals shown in Figure 6 are certainly consistent with the proposal that this should be an effective exchange pathway. We note at this point that several authors have argued that linear NNN couplings (M–O–M’–O–M) play a significant role in the magnetism of perovskite systems.<sup>4,5</sup> In the present case, this would correspond to coupling between Ir centers separated by an intervening {O–Fe–O} unit and between Fe centers separated by an intervening {O–Ir–O} unit,  $J_5$  and  $J_6$ , respectively, in Figure 7. By extending our unit cell to a  $2\sqrt{2} \times 2\sqrt{2} \times 1$  expansion of the unit cell containing 16  $\text{Fe}^{2+}$

and 16  $\text{Ir}^{2+}$  ions, we have been able to include these terms in the Hamiltonian (supporting information, Figure S8). However these additional terms offer only a very marginal improvement in terms of quality of fit and the best-fit parameter set  $\{J_1 = -46.4 \text{ cm}^{-1}, J_2 = -5.3 \text{ cm}^{-1}, J_3 = -230.7 \text{ cm}^{-1}, J_4 = +2.0 \text{ cm}^{-1}, J_5 = -0.3 \text{ cm}^{-1}, J_6 = -4.3 \text{ cm}^{-1}\}$  suggests that the last two are small in magnitude. We therefore find no evidence that these 3-bond couplings are physically significant in this particular system: the magnetic properties are instead dominated by  $J_1$  and  $J_3$ .

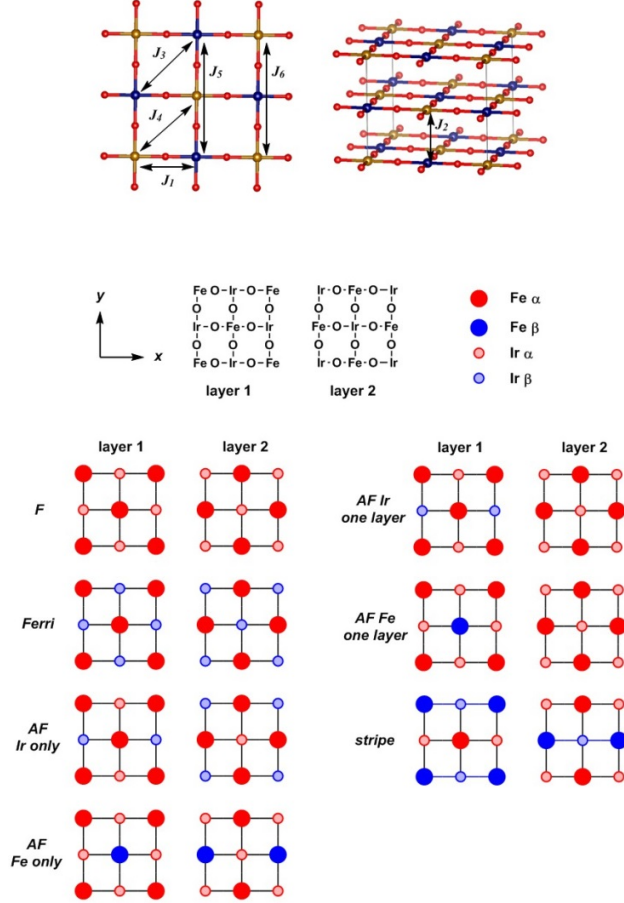


**Figure 7.** Exchange coupling pathways considered in the 4- and 6-parameter Heisenberg Hamiltonians (top) and the seven magnetic configurations used to compute the exchange coupling coefficients  $J_{1-4}$  (bottom). Brown, blue and red spheres represent Fe, Ir and O respectively in the top section.

**Magnetic frustration and magnetostriction.** As noted above, the dominant in-plane magnetic couplings in  $\text{Sr}_2\text{FeIrO}_4$  are the NN FeIr ( $J_1$ ) and NNN Ir-O $\cdots$ O-Ir ( $J_3$ ) interactions, both of which are strongly antiferromagnetic. These two couplings cannot be simultaneously satisfied to give a unique ground state: the strong antiferromagnetic coupling between NNN Ir ( $J_3$ ) is in direct competition with the antiferromagnetic NN FeIr ( $J_1$ ) coupling which will tend to impose a ferromagnetic arrangement between the two NNN Ir centers. As a result the system experiences a high-degree of spin frustration. The contribution of the individual exchange pathways to the total energy is given by  $J_3 S_{\text{Ir}} S_{\text{Ir}} = -236.0 \times 1/2 \times 1/2 = -59.0 \text{ cm}^{-1}$

per Ir-O $\cdots$ O-Ir pair vs  $J_1 S_{\text{Fe}} S_{\text{Ir}} = -44.7 \times 2 \times 1/2 = -44.7 \text{ cm}^{-1}$  per Fe-Ir pair, confirming that the two competing exchange couplings are indeed very finely balanced as well as being geometrically frustrated in a tetragonal lattice. On this basis, we propose that in the range  $115 < T/\text{K} < 300$  competition between  $J_1$  and  $J_3$  suppresses the onset of magnetic order, until this frustration is lifted by a structural distortion which breaks the tetragonal symmetry of the lattice.

The principal difference between the structures of  $\text{Sr}_2\text{FeIrO}_4$  at 150 K and below  $T \sim 100$  K is that the coordination geometry about the transition metal ions is no longer 4-fold symmetric at low temperature: two distinct mutually *trans* pairs of Ir-O and Fe-O bonds emerge. The difference between short and long Ir-O bond lengths (1.989(7) Å and 2.026(7) Å) leads to a distinct diamond-like distortion of the  $\text{IrO}_4$  squares. In terms of the magnetic structure discussed above, this orthorhombic distortion breaks the 4-fold rotational symmetry and differentiates the  $x$  and  $y$  directions, relieving the magnetic frustration between the homo-metallic ( $J_3$ ) and hetero-metallic ( $J_1$ ) couplings that is inherent in the symmetric structure. In Figure 3(c) we have plotted a bond distortion index, defined as the difference between the two bonds divided by their average value  $(\text{M-O}(1) - \text{M-O}(2)) / (0.5 \times (\text{M-O}(1) + \text{M-O}(2))) \times 100$ , the value of which is  $\sim 1.5\%$  for the Ir-O bonds at 1.5 K. Upon warming to 100 K, this bond distortion index drops in parallel with the decline in the ordered magnetic moment, to the point where both are indistinguishable from zero above 100 K (Figure 3). In order to further probe the origins of these structural distortions, we have carried out a further series of calculations (using the smaller  $\sqrt{2} \times \sqrt{2} \times 1$  expansion of the high-temperature tetragonal unit cell) where we allow the positions of the ions and the lattice parameters to relax subject to the constraint that the unit cell volume remains constant. In the absence of magnetostriction we would not anticipate any driving force for distortions of the type seen in the 1.5 K neutron diffraction data, simply because neither  $\text{Fe}^{2+}$  nor  $\text{Ir}^{2+}$  is orbitally degenerate in its ground state configuration. Indeed we find that in the ferrimagnetic configuration where all NN Fe-Ir couplings are antiferromagnetic (“*ferri*” in Figure 7), the converged lattice is almost perfectly tetragonal, with lattice vectors of almost equal length along the  $x$  and  $y$  directions ( $a = 7.998$  Å,  $b = 7.995$  Å,  $c = 7.026$  Å) and four identical M-O bonds around each metal (1.986 Å and 2.013 Å for Fe-O and Ir-O respectively). If, however, we impose the “*stripe*” magnetic configuration shown in Figure 7 (*i.e.* the configuration revealed by the 1.5 K neutron diffraction data) the relaxed lattice is distinctly orthorhombic ( $a = 7.959$  Å,  $b = 8.029$  Å,  $c = 7.030$  Å) with M-O bond lengths that split into distinct pairs (Fe-O = 1.971/1.999 Å, Ir-O = 2.009/2.016 Å). These observations offer strong support for the proposal that the structural distortion and the onset of magnetic order are intimately coupled.

The magnetic configuration shown in Figure 5 reveals one further subtlety relating the magnetic ordering along  $c$ : the preference for antiferromagnetic coupling of the separate Fe and Ir lattices also causes frustration along  $c$ , with each metal ion sandwiched between two nearest neighbors (above and below) with different spins. This frustration should provide a further driving force for magnetostriction which would take the form of an alternation of long and short inter-layer separations, and a further lowering of the crystal symmetry to  $P112$ ,

a polar space group. However, refinement of a  $P112$  symmetry structural model against the low-temperature neutron diffraction data gave fits which are statistically equivalent to the  $I112/m$  model, and all the interlayer distances are equal, within error. This suggests that if there is a further lowering of structural symmetry to  $P112$ , the atom displacements associated with this are too small to be observed in our data. The question of long-range ordering along  $c$  is intrinsically beyond the scope of the  $\sqrt{2} \times \sqrt{2} \times 1$  superlattice used in our computational model, where only two layers are present in the unit cell. However, calculations on an extended  $\sqrt{2} \times \sqrt{2} \times 2$  superlattice reveal that the energetic differences between alternative alignments along  $c$  are very small (of the order of 0.01 eV per formula unit), as might be expected given the  $\sim 3.5$  Å separation between the metal ions. Thus both experiment and theory concur that the frustration along  $c$  is not sufficient to drive a detectable magnetostriction in this direction.

## Conclusions

In this paper we have shown that the reaction between  $\text{Sr}_2\text{FeIrO}_6$  and dilute hydrogen leads to the formation of  $\text{Sr}_2\text{FeIrO}_4$  via a topochemical reaction. This novel phase consists of an array of square-planar  $\text{Fe}^{2+}\text{O}_4$  and  $\text{Ir}^{2+}\text{O}_4$  units connected via common oxide ions to form infinite sheets, which are stacked with layers of  $\text{Sr}^{2+}$  cations. The Fe and Ir centers are ordered in an arrangement inherited from the parent  $\text{Sr}_2\text{FeIrO}_6$  phase as shown in Figure 1. DFT calculations performed in a plane-wave basis suggest that the metal ions adopt high-spin  $\text{Fe}^{2+}$  ( $d^6$ ,  $S = 2$ ) and low-spin  $\text{Ir}^{2+}$  ( $d^7$ ,  $S = 1/2$ ) states, respectively. Moreover, the calculations confirm that both ions have a doubly occupied  $d_{z^2}$  orbital, a feature that is emerging as a consistent feature of all layered oxide phases of this type. The stability and double occupation of  $d_{z^2}$  in the  $\text{Ir}^{2+}$  ions invites a somewhat unexpected analogy to the extensively studied iridate ion ( $\text{Ir}^{4+}$ ) because both ions share a common near-degenerate ( $d_{xy/xz/yz}$ )<sup>5</sup> valence configuration. The low-symmetry tetragonal field lifts the degeneracy of the  $d_{xy/xz/yz}$  manifold, with  $d_{xy}$  singly occupied in the non-relativistic calculation, but the introduction of spin-orbit coupling effectively remixes the three  $d$  orbitals in a  $J_{1/2}$  ground state.

Low-temperature ( $< 115$  K) neutron diffraction data reveal that the Ir and Fe sublattices adopt type II antiferromagnetically coupled networks which interpenetrate each other leading to frustration in the nearest-neighbor Fe-O-Ir couplings, half of which are ferromagnetic and half anti-ferromagnetic. The spin frustration provides a driving force for symmetry-lowering structural distortion in which the four equivalent Ir-O and Fe-O distances of the tetragonal lattice split into two mutually trans pairs in a lattice with monoclinic symmetry. This strong magneto-lattice coupling arises from the novel local electronic configurations of the  $\text{Fe}^{2+}$  and  $\text{Ir}^{2+}$  cations and their cation-ordered arrangement in a distorted perovskite lattice.

## ASSOCIATED CONTENT

Details of the chemical, magnetic and crystallographic characterization of  $\text{Sr}_2\text{FeIrO}_4$ . Details of the computational methods and calculation of the exchange coupling constants,  $J_{1-6}$ . This material is available free of charge via the Internet at <http://pubs.acs.org>.

## AUTHOR INFORMATION

### Corresponding Author

michael.hayward@chem.ox.ac.uk

### Author Contributions

The manuscript was written through contributions of all authors. The authors declare no competing financial interests.

## ACKNOWLEDGMENT

We thank The Leverhulme Trust grant award RPG-2014-366 “Topochemical reduction of 4d and 5d transition metal oxides” for supporting this work. Experiments at the Diamond Light Source were performed as part of the Block Allocation Group award “Oxford Solid State Chemistry BAG to probe composition-structure-property relationships in solids” (EE13284). Experiments at the ISIS pulsed neutron facility were supported by a beam time allocation from the STFC.

## REFERENCES

- Vasala, S.; Karppinen, M.,  $\text{A}_2\text{B}'\text{B}''\text{O}_6$  perovskites: a review. *Prog. Solid St. Chem.* **2015**, *43*, 1-36.
- Kobayashi, K. I.; Kimura, T.; Tomioka, Y.; Sawada, H.; Terakura, K.; Tokura, Y., Intergrain tunneling magnetoresistance in polycrystals of the ordered double perovskite  $\text{Sr}_2\text{FeReO}_6$ . *Phys. Rev. B* **1999**, *59*, 11159-11162.
- Kato, H.; Okuda, T.; Okimoto, Y.; Tomioka, Y.; Takenoya, Y.; Ohkubo, A.; Kawasaki, M.; Tokura, Y., Metallic ordered double-perovskite  $\text{Sr}_2\text{CrReO}_6$  with maximal Curie temperature of 635 K. *Appl. Phys. Lett.* **2002**, *81*, 328-330.
- Kanungo, S.; Yan, B. H.; Jansen, M.; Felser, C., Ab initio study of low-temperature magnetic properties of double perovskite  $\text{Sr}_2\text{FeOsO}_6$ . *Phys. Rev. B* **2014**, *89*, 214414.
- Morrow, R.; Mishra, R.; Restrepo, O. D.; Ball, M. R.; Windl, W.; Wurmehl, S.; Stockert, U.; Buchner, B.; Woodward, P. M., Independent ordering of two interpenetrating magnetic sublattices in the double perovskite  $\text{Sr}_2\text{CoOsO}_6$ . *J. Am. Chem. Soc.* **2013**, *135*, 18824-18830.
- Ou, X. D.; Li, Z. W.; Fan, F. R.; Wang, H. B.; Wu, H., Long-range magnetic interaction and frustration in double perovskites  $\text{Sr}_2\text{NiIrO}_6$  and  $\text{Sr}_2\text{ZnIrO}_6$ . *Scientific Reports* **2014**, *4*, 7542:1-4.
- Woodward, P. M., Octahedral tilting in perovskites .1. Geometrical considerations. *Acta Crystallogr. Sect. B-Struct. Commun.* **1997**, *53*, 32-43.
- Glazer, A. M., Classification of tilted Octahedra in Perovskites. *Acta Crystallogr. Sect. B-Struct. Commun.* **1972**, *B 28*, 3384-3392.
- Morrow, R.; Freeland, J. W.; Woodward, P. M., Probing the links between structure and magnetism in  $\text{Sr}_{2-x}\text{Ca}_x\text{FeOsO}_6$  double perovskites. *Inorg. Chem.* **2014**, *53*, 7983-7992.
- De Teresa, J. M.; Serrate, D.; Blasco, J.; Ibarra, M. R.; Morellon, L., Impact of cation size on magnetic properties of  $(\text{AA}')_2\text{FeReO}_6$  double perovskites. *Phys. Rev. B* **2004**, *69*, 144401.
- Kato, H.; Okuda, T.; Okimoto, Y.; Tomioka, Y.; Oikawa, K.; Kamiyama, T.; Tokura, Y., Metal-insulator transition of ferromagnetic ordered double perovskites:  $(\text{Sr}_{1-y}\text{Ca}_y)_2\text{FeReO}_6$ . *Phys. Rev. B* **2002**, *65*, 144404.
- Dixon, E.; Hadermann, J.; Ramos, S.; Goodwin, A. L.; Hayward, M. A., Mn(II) in an extended oxide: the synthesis and characterization of  $\text{La}_{1-x}\text{Ca}_x\text{MnO}_{2+d}$  ( $0.6 \leq x \leq 1$ ). *J. Am. Chem. Soc.* **2011**, *133*, 18397-18405.
- Hayward, M. A.; Green, M. A.; Rosseinsky, M. J.; Sloan, J., Sodium hydride as a powerful reducing agent for topotactic oxide deintercalation: synthesis and characterisation of the nickel (II) oxide  $\text{LaNiO}_2$ . *J. Am. Chem. Soc.* **1999**, *121*, 8843-8854.



14. Seddon, J.; Suard, E.; Hayward, M. A., Topotactic reduction of  $\text{YBaCo}_2\text{O}_5$  and  $\text{LaBaCo}_2\text{O}_5$ : square-planer Co(I) in an extended oxide. *J. Am. Chem. Soc.* **2010**, *132*, 2802-2810.
15. Denis Romero, F.; Burr, S. J.; McGrady, J. E.; Gianolio, D.; Cibin, G.; Hayward, M. A.,  $\text{SrFe}_{0.5}\text{Ru}_{0.5}\text{O}_2$ : square-planar  $\text{Ru}^{2+}$  in an extended oxide. *J. Am. Chem. Soc.* **2013**, *135*, 1838-1844.
16. Tsujimoto, Y.; Tassel, C.; Hayashi, N.; Watanabe, T.; Kageyama, H.; Yoshimura, K.; Takano, M.; Ceretti, M.; Ritter, C.; Paulus, W., Infinite-layer iron oxide with a square-planar coordination. *Nature* **2007**, *450*, 1062-1065.
17. Amano Patino, M.; Zeng, D.; Bower, R.; McGrady, J. E.; Hayward, M. A., Coupled electronic and magnetic phase transition in the infinite-layer phase  $\text{LaSrNiRuO}_4$ . *Inorg. Chem.* **2016**, *55*, 9012-9016.
18. Page, J. E.; Topping, C. V.; Scrimshire, A.; Bingham, P. A.; Blundell, S. J.; Hayward, M. A., Doped  $\text{Sr}_2\text{FeIrO}_6$  – phase separation and a  $J_{\text{eff}} \neq 0$  state for  $\text{Ir}^{5+}$ . *Inorg. Chem.* **2018**, DOI:10.1021/acs.inorgchem.8b01539.
19. Battle, P. D.; Blake, G. R.; Gibb, T. C.; Vente, J. F., Structural chemistry and electronic properties of  $\text{Sr}_2\text{FeIrO}_6$ . *J. Solid State Chem.* **1999**, *145*, 541-548.
20. Larson, A. C.; Von Dreele, R. B. *General Structure Analysis System*, Los Alamos National Laboratory Report LAUR 86-748: 2000.
21. Kresse, G.; Furthmüller, J., Efficient iterative schemes for ab initio total-energy calculations using a plane-wave basis set. *Phys. Rev. B* **1996**, *54*, 11169-11186.
22. Kresse, G.; Hafner, J., Ab-initio molecular-dynamics for liquid-metals. *Phys. Rev. B* **1993**, *47*, 558-561.
23. Perdew, J. P.; Burke, K.; Wang, Y., Generalized gradient approximation for the exchange-correlation hole of a many-electron system. *Phys. Rev. B* **1996**, *54*, 16533-16539.
24. Blochl, P. E., Projector augmented-wave method. *Phys. Rev. B* **1994**, *50*, 17953-17979.
25. Dudarev, S. L.; Botton, G. A.; Savrasov, S. Y.; Humphreys, C. J.; Sutton, A. P., Electron-energy-loss spectra and the structural stability of nickel oxide: An LSDA+U study. *Phys. Rev. B* **1998**, *57*, 1505-1509.
26. Monkhorst, J. J.; Pack, J. D., Special points for Brillouin zone integrations. *Phys. Rev. B* **1976**, *13*, 5188-5192.
27. Hobbs, D.; Kresse, G.; Hafner, J., Fully unconstrained noncollinear magnetism within the projector augmented-wave method. *Phys. Rev. B* **2000**, *62*, 11556-11570.
28. Garcia, M. P.; Jimenez, M. V.; Oro, L. A.; Lahoz, F. J.; Alonso, P. J., A paramagnetic, mononuclear organometallic Ir(II) complex -  $\text{Ir}(\text{C}_6\text{Cl}_5)_2(\text{COD})$ . *Angew. Chem., Int. Ed.* **1992**, *31*, 1527-1529.
29. Garcia, M. P.; Jimenez, M. V.; Oro, L. A.; Lahoz, F. J.; Tiripicchio, M. C.; Tiripicchio, A., A homoleptic mononuclear Ir(II) organometallic complex - synthesis and X-ray structure of  $\text{Ir}(\text{C}_6\text{Cl}_5)_4$ . *Organometallics* **1993**, *12*, 4660-4663.
30. Meiners, J.; Scheibel, M. G.; Lemee-Cailleau, M. H.; Mason, S. A.; Boeddinghaus, M. B.; Fassler, T. F.; Herdtweck, E.; Khusniyarov, M. M.; Schneider, S., Square-planar iridium(II) and iridium(III) amido complexes stabilized by a PNP pincer ligand. *Angew. Chem., Int. Ed.* **2011**, *50*, 8184-8187.
31. Pandey, K. K., Mononuclear  $d^7$  complexes of platinum metals. *Coordination Chemistry Reviews* **1992**, *121*, 1-42.
32. Campbell, B. J.; Stokes, H. T.; Tanner, D. E.; Hatch, D. M., ISODISPLACE: a web-based tool for exploring structural distortions. *J. Appl. Crystallogr.* **2006**, *39*, 607-614.
33. Kobayashi, K.; Nagao, T.; Ito, M., Radial integrals for the magnetic form factor of 5d transition elements. *Acta Crystallographica Section A* **2011**, *67*, 473-480.
34. Pruneda, J. M.; Iniguez, J.; Canadell, E.; Kageyama, H.; Takano, M., Structural and electronic properties of  $\text{SrFeO}_2$  from first principles. *Phys. Rev. B* **2008**, *78*, 115101.
35. Kanungo, S.; Mogare, K.; Yan, B. H.; Reehuis, M.; Hoser, A.; Felser, C.; Jansen, M., Weak orbital ordering of Ir t(2g) states in the double perovskite  $\text{Sr}_2\text{CeIrO}_6$ . *Phys. Rev. B* **2016**, *93*, 245148.
36. Kim, B. J.; Jin, H.; Moon, S. J.; Kim, J. Y.; Park, B. G.; Leem, C. S.; Yu, J.; Noh, T. W.; Kim, C.; Oh, S. J.; Park, J. H.; Durairaj, V.; Cao, G.; Rotenberg, E., Novel  $J(\text{eff})=1/2$  Mott state induced by relativistic spin-orbit coupling in  $\text{Sr}_2\text{IrO}_4$ . *Phys. Rev. Lett.* **2008**, *101*, 076402.
37. Cao, G.; Subedi, A.; Calder, S.; Yan, J. Q.; Yi, J. Y.; Gai, Z.; Poudel, L.; Singh, D. J.; Lumsden, M. D.; Christianson, A. D.; Sales, B. C.; Mandrus, D., Magnetism and electronic structure of  $\text{La}_2\text{ZnIrO}_6$  and  $\text{La}_2\text{MgIrO}_6$ : Candidate  $J(\text{eff})=1/2$  Mott insulators. *Phys. Rev. B* **2013**, *87*, 155136.
38. Son, W. J.; Manuel, P.; Adroja, D.; Whangbo, M. H., Density Functional Analysis of the Magnetic Structure of  $\text{Li}_3\text{RuO}_4$ : Importance of the Ru-O center dot center dot center dot O-Ru Spin-Exchange Interactions and Substitutional Ru Defects at the Li Sites. *Inorg. Chem.* **2011**, *50*, 9400-9405.
39. Whangbo, M. H.; Koo, H. J.; Dai, D., Spin exchange interactions and magnetic structures of extended magnetic solids with localized spins: theoretical descriptions on formal, quantitative and qualitative levels. *J. Solid State Chem.* **2003**, *176*, 417-481.
40. Goodenough, J. B., *Magnetism and the chemical bond*. Wiley: New York, 1963.

**For Table of Contents Only.** Topochemical reduction of the double-perovskite oxide  $\text{Sr}_2\text{FeIrO}_6$  leads to the formation of  $\text{Sr}_2\text{FeIrO}_4$  - a phase consisting of ordered infinite sheets of apex-linked  $\text{Fe}^{2+}\text{O}_4$  and  $\text{Ir}^{2+}\text{O}_4$  squares. On cooling below 115 K  $\text{Sr}_2\text{FeIrO}_4$  enters a magnetically ordered state in which the  $\text{Ir}^{2+}$  ( $d^7$ ,  $S = 1/2$ ) and  $\text{Fe}^{2+}$  ( $d^6$ ,  $S = 2$ ) sub-lattices adopt antiferromagnetically coupled networks, leading to frustration in the nearest-neighbor Fe-O-Ir couplings which drives a structural distortion which lowers the lattice symmetry.

---

